(This is a sample cover image for this issue. The actual cover is not yet available at this time.)

Journal of African Earth Sciences 66-67 (2012) 22–34

Contents lists available at SciVerse ScienceDirect

Journal of African Earth Sciences

journal homepage: www.elsevier.com/locate/jafrearsci

Integrating geologic and satellite imagery data for high-resolution mapping and gold exploration targets in the South Eastern Desert, Egypt

Basem Zoheir[a,*], Ashraf Emam[b]

[a] Department of Geology, Faculty of Science, Benha University, Benha 13518, Egypt
[b] Geology Department, Aswan Faculty of Science, South Valley University, Aswan 81528, Egypt

ARTICLE INFO

Article history:
Received 20 August 2011
Received in revised form 21 February 2012
Accepted 23 February 2012
Available online 7 March 2012

Keywords:
ETM+ and ASTER data
Greenstone belts
Gold exploration targets
South Eastern Desert
Egypt

ABSTRACT

The granitoid-greenstone belts of the Arabian–Nubian Shield are well-endowed with lode gold and massive sulfide ores. Although generally characterized by excellent outcrops and arid desert realm, poor accessibility and lack of finance have been always retardant to detailed geologic mapping of vast areas of the shield. Lack of comprehensive geological information and maps at appropriate scales would definitely hinder serious exploration programs.

In this study, band ratioing, principal component analysis (PCA), false-color composition (FCC), and frequency filtering (FFT-RWT) of ASTER and ETM+ data have substantially improved visual interpretation for detailed mapping of the Gebel Egat area in South Eastern Desert of Egypt. By compiling field, petrographic and spectral data, controls on gold mineralization have been assessed in terms of association of gold lodes with particular lithological units and structures. Contacts between foliated island arc metavolcanics and ophiolites or diorite are likely to be favorable loci for auriferous quartz veins, especially where the NW–SE foliation is deflected into steeply dipping NNW-trending shear planes. High-resolution mapping of the greenstone belt, structures and alteration zones associated with gold lodes in the study area suggests that dilatation by foliation deflection was related to emplacement of the Egat granitic intrusion, attendant with a sinistral transpression regime (i.e., ~640–550 Ma?). Gold mineralization associated with granitoid intrusions in transpression-induced pull-apart structures elsewhere in the Eastern Desert (e.g., Fawakhir, Sukari and Hangaliya mines) emphasize the reliability of this setting as a model for gold exploration targets in greenstone terrains of Egypt, and may be elsewhere in the Arabian–Nubian Shield.

1. Introduction

Greenstone belts are zones of variably metamorphosed ultramafic, volcanic and sedimentary rocks that occur within Archaean and Proterozoic cratons between granite and gneiss bodies (de Wit and Ashwal, 1995). Lode gold deposits, commonly hosted in greenstone belts, show a high degree of structural control (e.g., Ashley and Craw, 2004). The nature of this structural control depends on the tectonic setting, and crustal level at which mineralization has occurred (e.g., Hodgson, 1993; Groves et al., 1998; Bierlein and Crowe, 2000; Goldfarb et al., 2001). Deeper systems are typically hosted by ductile shear zones, whereas, shallower systems are hosted by brittle structures (e.g., Groves et al., 1998; Craw et al., 1999).

Widespread brittle–ductile shear zones in the greenstone terrains across the South Eastern Desert of Egypt locally host silicification and carbonatization haloes that are commonly associated with significant Au–Cu mineralization (e.g., Osman and Dardir, 1989; Ramadan et al., 2001; Kusky and Ramadan, 2002; Ramadan and Kontny, 2004; Gabr et al., 2010; Zoheir, 2011). The Wadi Allaqi district is characterized by discrete occurrences of small-scale (a few hundreds of meters-long), shear zone-associated auriferous quartz veins within ophiolitic-island arc metavolcanic terrains. Detailed and reconnaissance studies revealed significant gold grades (several ppms of Au) in hydrothermal alteration zones within and outside the old mining sites in the Wadi Allaqi region (e.g., Oweiss and Khalid, 1991; Kusky and Ramadan, 2002; Zoheir, 2008). The Gebel Egat (known also as Gebel Iqat, Gebel is the Arabic word for mountain) area (Fig. 1) is known for old mining sites for gold that were likely active during the early Islamic time (10th–11th century). A few studies attempted to provide information on geological and mineralogical features of gold mineralization in the area (Nasr et al., 1998; Oweiss and Said, 2000; Salem, 2007), while Zoheir et al. (2008) used fluid inclusion data to argue for an orogenic nature of the auriferous lodes in the Egat mine area.

The present contribution uses an integrated analysis of satellite imagery, mineralogical and structural data to understand the controls on gold mineralization in the Gebel Egat area. It reports on image processing and enhancement of ASTER and ETM+ data for

* Corresponding author.
E-mail address: basem.zoheir@gmail.com (B. Zoheir).

1464-343X/$ - see front matter © 2012 Elsevier Ltd. All rights reserved.
http://dx.doi.org/10.1016/j.jafrearsci.2012.02.007

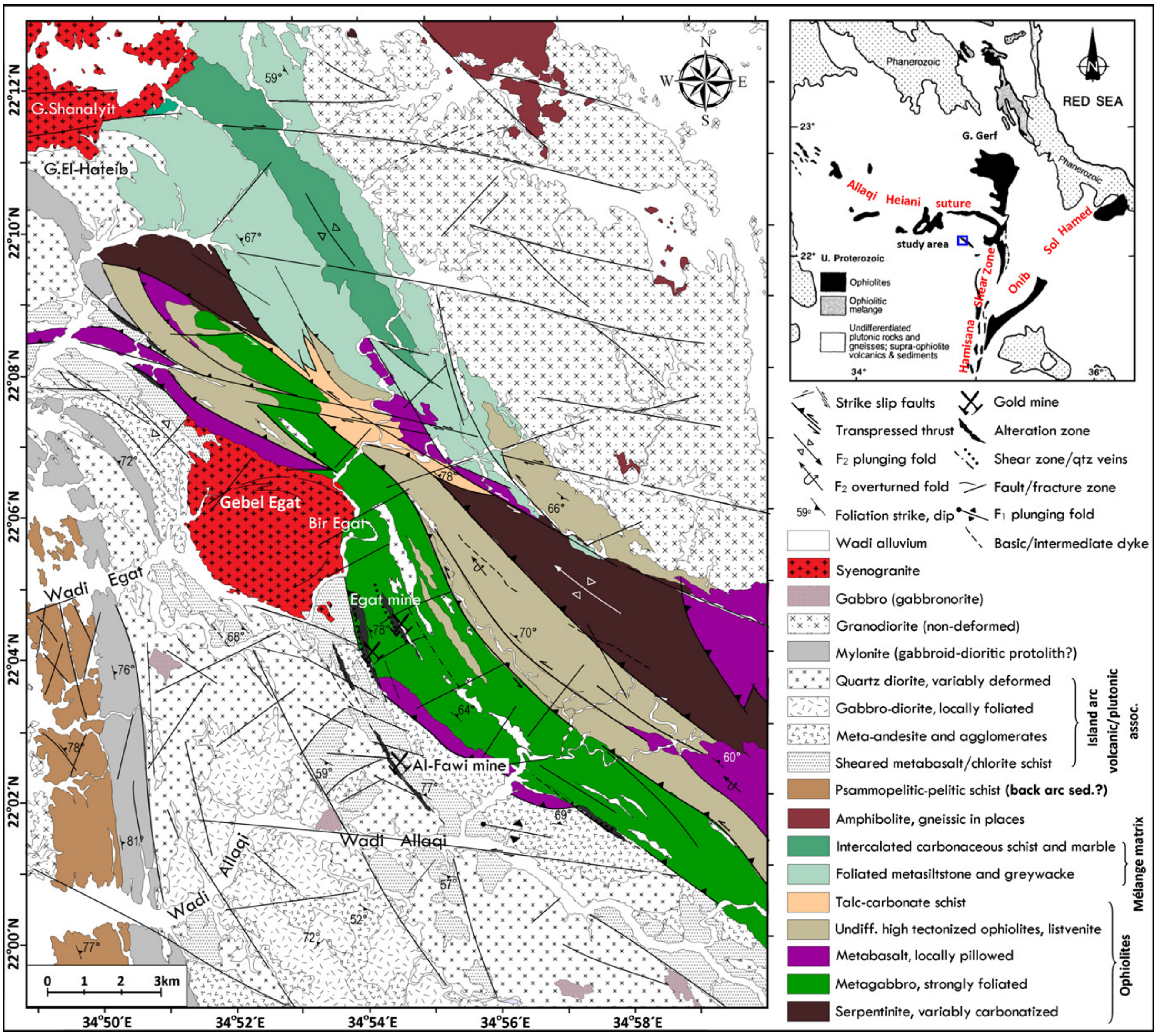

Fig. 1. Geological and structural elements exposed in the Egat and Al-Fawi mining sites within the Wadi Allaqi region, compiled from integrated field, petrographic and satellite imagery data analysis. Inset showing the location of the Gebel Egat area within the Allaqi-Heiani-Onib-Sol Hamed belt and Hamisana Shear zone.

high-resolution geological mapping, and locating potential gold exploration targets along the major lineaments that accommodate already known mining sites.

2. Geologic setting

The Gebel Egat area is part of the Neoproterozoic Allaqi-Heiani belt in the South Eastern Desert of Egypt (Fig. 1). A highly tectonized, strongly foliated NW–SE-trending belt of interlayered ophiolites and island arc metavolcanic/volcaniclastic rocks dominates the area. This belt is cut by sheared and non-deformed granitoids intrusions, of which the most conspicuous is Gebel Egat (Fig. 2a). Elongated sheets and slices of ophiolites are tectonically stacked south-westwards and thrusted over foliated island arc metavolcanic rocks.

The ophiolitic rocks include serpentinite, metagabbro, metabasalt, and their highly sheared and metasomatized derivatives. The latter include talc-carbonate schist and listvenite or listvenitized serpentinite (Fig. 2b). Serpentinite is composed of antigorite, chrysotile and subordinate talc, dolomite, ankerite, magnetite, chromite and tremolite. Relic olivine and pyroxene grains are rare. Metagabbro constitutes a major part of the ophiolitic belt in the study area. Close to Bir Egat, kinematic indicators, e.g., releasing bends and asymmetric porphyroblasts, in strongly foliated metagabbro indicate a left-lateral sense of shear (Fig. 2c). Metagabbro is composed chiefly of plagioclase, actinolitic hornblende, together with subordinate clinopyroxene. Sphene, apatite and titanomagnetite are accessory minerals. Chlorite, actinolite, epidote and less common calcite indicate low-grade metamorphism. The contact zone between metagabbro and serpentinite is defined by steeply-dipping thrust structures, locally imposed by tight to isoclinal folds. Metabasalt is less common than serpentinite and metagabbro. Its poorly defined, pillowed morphology is variably obliterated by deformation. Metabasalt is composed of plagioclase, pyroxene, actinolite and minor sphene and magnetite. Undifferentiated, highly tectonized ophiolites and talc-carbonate schist define the thrust zones, where talc pockets are stretched along the thrust planes. Listvenite and/or listventized ophiolites form an elongated

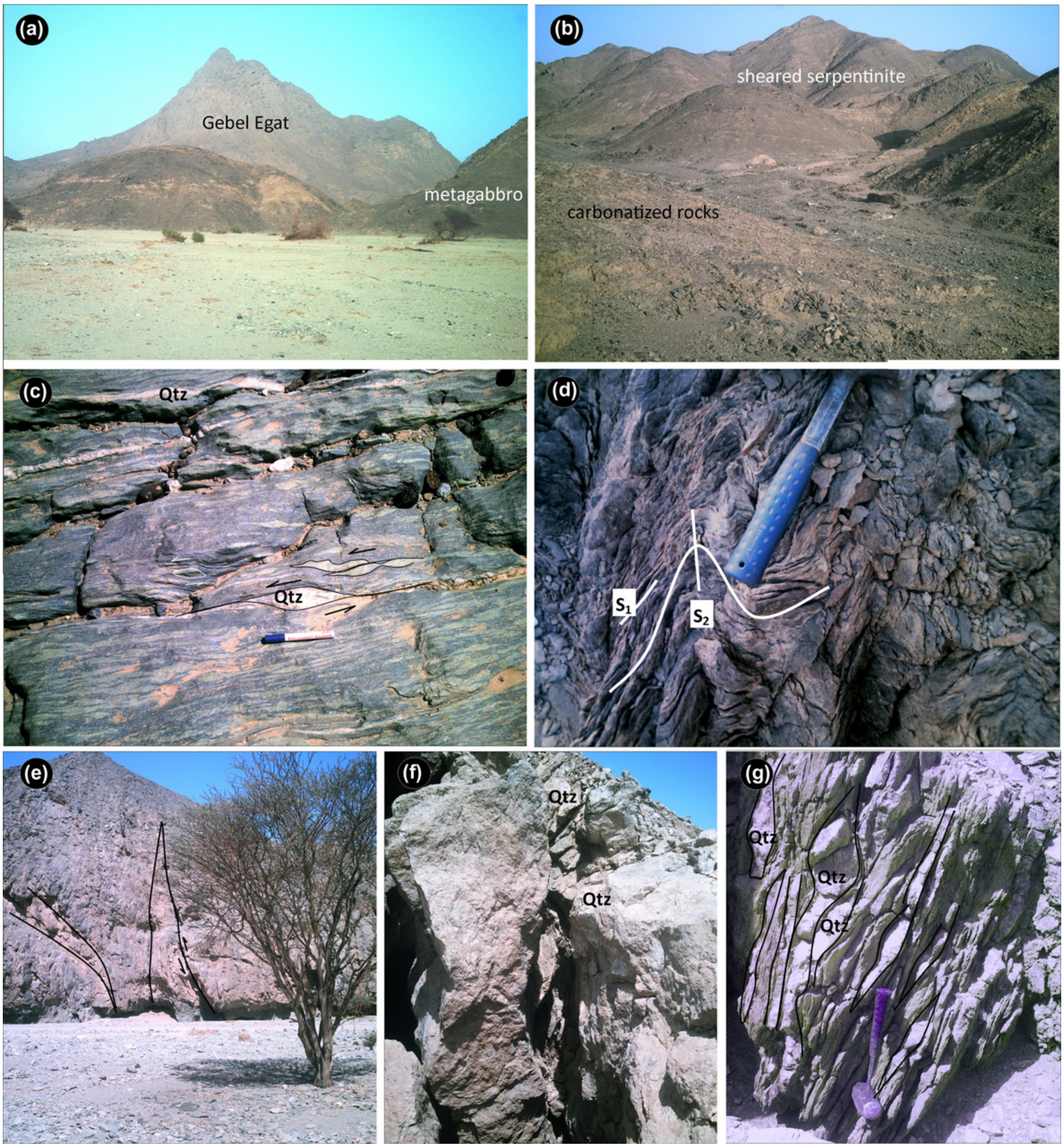

Fig. 2. Geological features at the Gebel Egat area. (a) Gebel Egat grainitic intrusion cuts the NW-trending, interlayered highly foliated ophiolitic metagabbro and metavolcanics [Photo looking N], (b) Exposures of steeply-dipping, highly cleaved metagabbro and variably carbonatized, listvenitized serpentinite rocks close to Egat mine [Photo looking NE], (c) Quartz-filled releasing bents, stretched grains and sinisterly slipped porphyroblasts in strongly foliated metagabbro near Egat water well, (d) S_2 imposed on S_1 foliation in carbonatized ophiolites within the mine area, (e) Steeply dipping and inclined silicified shear zones close to the thrust contact between ophiolites and island arc metavolcanic rocks [Photo looking N], (f) Stopped out quartz pods and silicified and carbonatized rocks, sub-parallel to the host rock foliation [Photo looking N], (g) Highly deformed quartz boudins, pinched-and-swelled within anastomosing shear zones in Egat mine [Photo looking NW].

slab in the north-eastern part of the study area, and could be a product of K-metasomatism by the large granodiorite intrusion (see Fig. 1). Finely foliated metasiltstone, metagraywacke and carbonaceous schists form the mélange matrix in which the large ophiolitic blocks are embedded. The interlayered carbonaceous schist and marble form a NNW-trending synform in the northern part of the study area.

Amphibolite occurs as a roof-pendant in granodiorite in the northern part of the study area. Amphibolite is a medium- to coarse-grained, highly-foliated rock, composed essentially of hornblende, actinolite and plagioclase. Disseminated garnet is seen in some samples, and zircon and apatite become common in places. A banded or gneissic appearance is locally well-developed, suggesting high metamorphic grades. A para- or ortho-origin cannot be determined since relict features become more difficult to recognize with increasing metamorphic grade. However, the amphibolite rocks extend farther north than the study area and are associated with pelitic metasediments of back arc origin (Zoheir, 2004). This association may suggest a para-origin. Highly deformed sequences of staurolite- and sillimanite-bearing biotite-schists form a ~N-trending belt, characterized by vertical foliation, parallel to major shear zones in the western part of the study area. These rocks form a narrow belt (~2 km-wide) extending to the north for more than 20 km. Island arc, basic to intermediate metavolcanic/volcaniclastic assemblages occur in the southern part of the study area as medium-grained, porphyroblastic rocks, generally foliated in a NW–SE direction. These rocks have mainly metabasalt or meta-andesite compositions. Tuffs and agglomerates are less common, and are locally intercalated with metabasalt bands. The island arc rocks are cut by discrete gabbro–granitoid intrusions. Chlorite, actinolite and epidote imply metamorphism under greenschist facies conditions. Nasr et al. (1998) described a ~40 km-long (5–10 km-wide) belt of schistose volcaniclastic rocks confined to and controlled by the Al-Fawi-Egat shear zone. Salem (2007) described these rocks as metabasalt, meta-andesite and subordinate metadacite and tuffs.

Gabbro–diorite intrusions are likely island arc plutonic phases. These rocks exhibit variable degrees of deformation, from massive to strongly sheared or foliated. Their mineralogy includes clinopyroxene and amphibole, in addition to plagioclase and subordinate quartz, chlorite and titanomagnetite. Gabbro–diorite rocks are widespread in the southern part of the study area, where they are associated with island arc metavolcanic/volcaniclastic rocks. Quartz diorite occurs as medium-grained rock, composed essentially of plagioclase, hornblende, biotite, quartz and rare pyroxene. In the Egat mine area and southwards, elongated massed of quartz diorite cut the foliated metagabbro. East of G. Egat, coarse-grained granodiorite forms deeply eroded, low-lying isolated hills covered by sand deposits. While gabbro–diorite and quartz diorite are variably sheared/foliated, granodiorite shows no signs of deformation. Small, irregular intrusions of gabbronorite cut the quartz diorite terrain and have moderate relief. Gabbronorite is a medium-grained, melanocratic rock composed of calcic plagioclase, pyroxene and less abundant olivine. Sub-rounded intrusions of porphyritic monzo- to syenogranite cut the foliated ophiolitic and island arc rocks, and show no evidence of shearing. K-feldspar, biotite and quartz are their main constituents, while muscovite is subordinate and zircon is accessory. Basic and intermediate dykes cut most of the country rocks, and commonly trend NW and ENE.

3. Structural setting

The Gebel Egat area has experienced multiple phases of deformation manifested by superimposed structures, including from older to younger: (1) WNW-trending folds and antiforms (F_1) and related foliation (S_1), commonly developed in the island arc metavolcanic rocks; (2) NW- to NNW-trending, overturned folds (F_2) and steeply-dipping, SE-vergent thrust segments and crenulation cleavage (S_2), common in ophiolitic rocks; and (3) NNW-trending shear and mylonitic zones, quartz pods (Fig. 2d), conjugate sinistral NNW–SSE and dextral WNW–ESE strike-slip faults in the island arc and ophiolitic rocks everywhere in the study area (Table 1).

Moderately dipping S_1 foliation, preserved only in the island arc metavolcanics, is defined by alignment of mica and amphibole, and by elongated pyroclasts in agglomerate and by WNW-trending compositional banding in places. Approaching the thrust contacts with ophiolites S_1 foliation is kinked by a steeply dipping, axial planar crenulation cleavage (S_2). In the high strain domains, steeply-dipping S_2 foliation totally obliterates the S_1 foliation, especially where brittle–ductile shear zones are developed. A NNW-trending belt of highly deformed/mylonitized diorite and metasedimentary rocks in the western part of the study area defines a zone of locally strong ductile deformation. The latter is most likely a continuation of or a splay from the major Hamisana Zone farther south. Conjugate sinistral, NNW–SSE and dextral, WNW–ESE strike-slip faults deform all pre-existing structures and lithologies. Offset along the NNW-trending faults cannot be determined due to lack of good markers, but displacement along the WNW-trending faults measures up to 300 m in a right-lateral sense.

In view of the deformation history of the central part of the Allaqi-Heiani suture (Zoheir and Klemm, 2007 and reference therein), intense crustal shortening took place throughout the collision of east and west Gondwana (640–550 Ma; Table 1). As a result, the Allaqi-Heiani suture was deformed by the post-accretionary N–S trending Hamisana Zone and related NW–SE sinistral and NE–SW dextral transpressional faults, during the Late Pan-African Najd orogen (e.g., Abdeen and Abdelghaffar, 2011). Field observations and satellite data reveal that the WNW-trending, dextral strike-slip faults and shears do not affect the granitic mass of Gebel Egat, but imposed on the foliated country rocks around it. This may imply that emplacement of the Egat granite body took place in the late stages of wrenching along the conjugate system of WNW- and NNW-trending faults/shears zones. Features including its sub-rounded, NW-stretched shape and wrapping of the country rock foliation around the G. Egat intrusion further support this suggestion. Kinematic indicators of a long-lasting sinistral transpression regime include close to tight upright folds and abundant steeply dipping shear zones (at all scales). Development of the NNW-trending shear zones, which accommodate the gold-bearing quartz veins, is attributed to dilatation and distortion by the emplacement of the Gebel Egat intrusion into the steeply dipping foliation (Fig. 2e). Localization of the auriferous shear zones in distorted foliation and along contacts between different lithologies may be attributed to differential shear and rock competency.

4. Gold mineralization and associated hydrothermal alteration

Gold mineralization is confined to NNW–SSE, anastomosing shear zones and associated hydrothermal alteration in the metagabbro and island arc metavolcanics in Egat mine, and at contacts between the island arc metavolcanics and quartz diorite in the Al-Fawi mine (see Fig. 1; Fig. 2f and g). Zoheir et al. (2008) described mineralized quartz lenses (up to 3 m-wide) discontinuously over a distance of more than 1 km along brittle–ductile shear zones in the Egat mine area. Kinematic indicators within the shear zones, e.g., top-to-northwest stretching lineation, asymmetries and slickensides, suggest an oblique dip and slip movement. Sinistral shearing is identified from asymptotic curvature of foliation into the shear bands, and "S" asymmetry of mineralized quartz lenses. Morphology and microstructures of the mineralized quartz veins reveal pervasive ductile deformation and brecciation (Fig. 3a–f), suggesting syn-kinematic vein formation. Sinistral shearing and slip is seen in many samples, and grain boundary migration, bugling recrystallization and sub-grain development are common features in the ore shoots (Fig. 3a–d). Disseminated sulfides are common where chlorite, sericite and carbonate are intermingled (Fig. 3c–f).

In the Egat mine area, parallel to sub-parallel quartz veins and hydrothermal alteration haloes (~30–120 m-wide) extend for approximately 1.5 km. Hydrothermal alteration is more intense where dyke-like bodies of quartz diorite taper along the strongly foliated metagabbro (see Fig. 1). The alteration assemblage includes quartz, sericite, chlorite, carbonate, goethite and pyrite. Chlorite and pyrite in the altered wall rocks decrease away from the quartz veins more rapidly than sericite and carbonate. Remote sensing and field work identified three silicification zones within and close to the Egat-Al-Fawi mining area (Fig. 1). Along these alteration zones, several open pits and trenches into quartz veins and boudins have been seen. Although thick (>3 m-wide) quartz veins are more abundant in the western zone, the central zone gives the highest gold grade among the three zones (up to 10 g/t Au). Nasr et al. (1998) and Oweiss and Said (2000) reported up to ~12 g/t Au in grab samples from the intensely altered metavolcanic rocks in Egat mine area. The mineralized quartz veins contain disseminated pyrite and arsenopyrite, and minor amounts of chalcopyrite, pyrrhotite and galena. Pyrite and arsenopyrite appear to be largely restricted to thin selvages of the wall rock in the marginal parts. Fine-grained arsenopyrite commonly contains gold and chalcopyrite inclusions (<50 μm). Goethite and siderite are

Table 1
Schematic compilation of the deformational phases and magmatic activities in G. Egat area relative to evolution of other parts of the Allaqi–Heiani suture.

Stern (1994)	Kusky and Ramadan (2002)		Zoheir and Klemm (2007)		Gebel Egat area (Present work)
	Tectonic/deformation event	Structural evidence	Deformation	Fabrics	Deformation fabric
Greater Gondwana break-up ~550 Ma	D4: (650–550 Ma)	NE-striking strike slip faults–E–W fractures	–WNW–ESE, NNE–SSW and N–S joint/fracture sets		
Crustal shortening and escape tectonics ~640–550 Ma	D3: (650–550 Ma) Shortening related to collision of east and west Gondwana; tectonic escape toward oceanic free face to N along WNW striking Najd faults	WNW–ESE and NW–SE shear zones and open folds, crenulation cleavage, SC fabrics, sigmoidal foliation patterns	D3: E–W-compressional regime (post-accretionay, shortening/transpression)	– Discrete NNW-trending shear zones, commonly traversing the ophiolitic and island arc rocks – F_3 major and minor syncline and anticline structures developed in the ophiolitic and island arc rocks	(3) NNW–SSE shear and mylonitic zones, conjugate sinistral NNW–SSE and dextral WNW–ESE strike-slip faults that are likely components of the Hamisana Zone (640–550 Ma) farther south
				– S_3 (NNW–SSE) crenulation cleavage and kinks, coaxial with F_3 axial planes – Right-lateral strike slip faults crosscutting the former fabrics and dislocating the ophiolitic blocks	(2) NW- to NNW-trending, overturned folds (F_2) and steeply-dipping thrust segments bounding the ophiolitic rocks. Steeply dipping crenulation foliation (S_2) imposed on the pre-existing fabrics
			D2: NE–SW compressional regime (early-stage shortening)	– WNW- to NW- upright folds (F_2) –Penetrative slate foliation (S_2) – Rotated porphyroblasts with sinistral asymmetry, σ-type quartz porphyroblasts and detached quartz ribbons	(1) WNW-trending anticlines and antiforms (F_1), best-developed in the island arc metavolcanics, commonly with moderate dipping assymetric limbs and foliation (S_1)
Greater Gondwanaland assembly ~700 Ma *Continental collision* 750–650 Ma	D2: (750–720 Ma) Collision of Gerf and Gabgaba terranes; *(late stage)*	– Regional S-vergent thrusts; imbrication of arc/arc accretionary complex – W-plunging steeply N-dipping axial planar cleavage	D1: Fold-and-thrust system formation (terrane accretion)	–Recumbent S- or SE-vergent folds (F_1)	
Rodinia break-up (late stage) 870–690 Ma Seaf loor spreading, arc and back-arc basin formation, and terrane accretion	D1: (750–720 Ma) Collision of the Gerf and Gabgaba arc terranes: *(early stages)*	– E–W striking, steeply N-dipping axial planar cleavage – East plunging isoclinal folds			

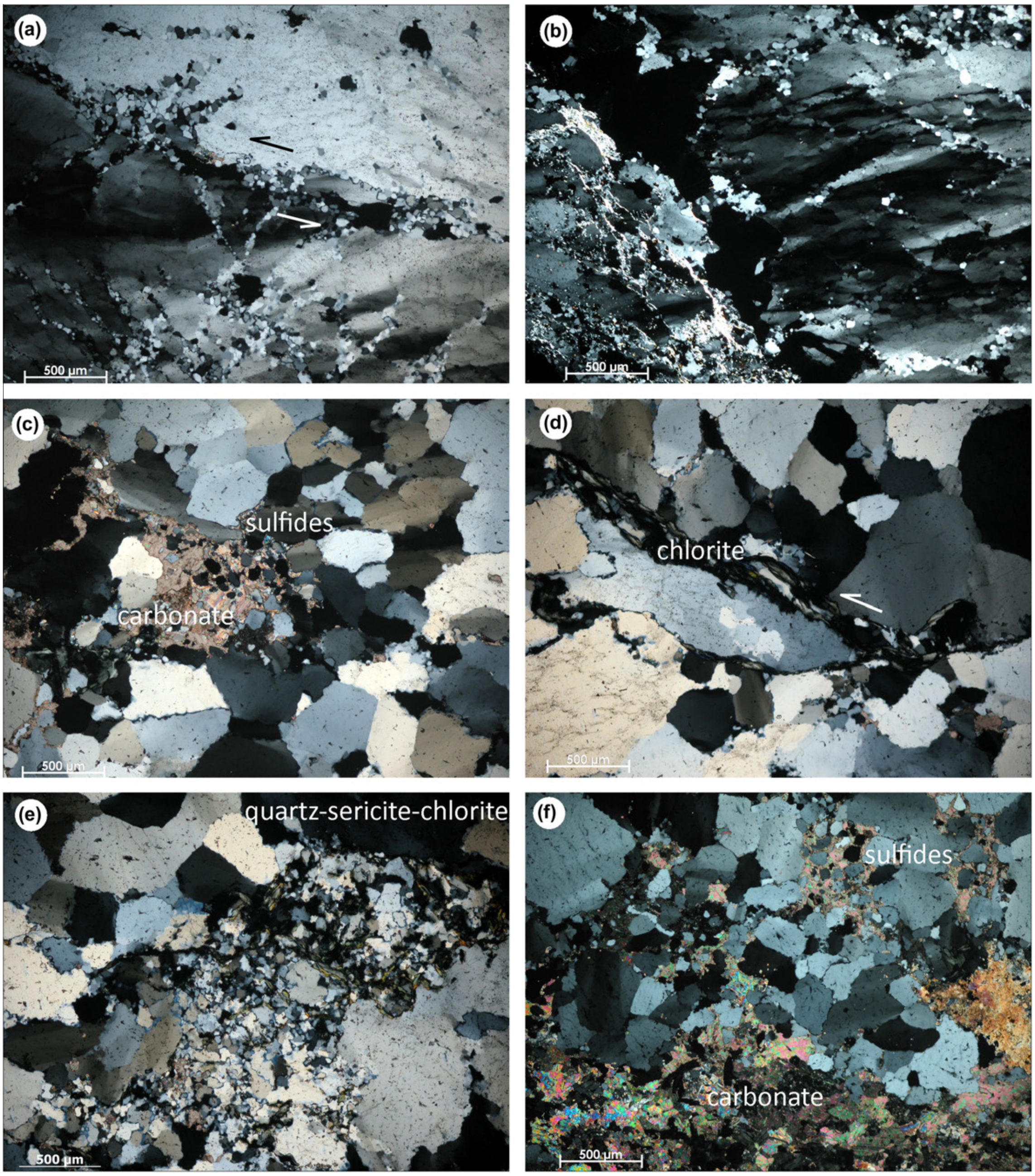

Fig. 3. Microscopic features of the mineralized quartz veins at Egat deposit. (a and b) Subgrain development (bugling recrystallization) along shear planes in strained vein quartz in gold lodes at Egat mine, (c and d) Disseminated sulfides, calcite and oriented chlorite flakes along serrate planes in mineralized quartz veins, and (e and f) Mosses of intergrown chlorite, sericite and carbonate along with microcrystalline quartz in gold lodes from Al-Fawi mine.

common in the weathered portions of the quartz veins and altered wall rocks. Dispersed specks of free gold (<20 μm) are common where arsenopyrite and pyrite are decomposed and severely oxidized. Gold grades in quartz veins range from traces to 40 g/t (Oweiss and Said, 2000). Gold in the Al-Fawi mine is related to shear-hosted, boudinaged and brecciated quartz veins along the fault contact between island arc metavolcanics and variably deformed quartz diorite. Quartz veins vary in width from 70 to 110 cm and extend for roughly 800 m along the shear zones (e.g., Salem, 2007). Stringers and veinlets of milky quartz are common in the intensely altered, locally pyritized metavolcanic rocks. Nasr et al. (1998) reported gold values of 0.5–11.2 g/t and 0.5–15 g/t in grab samples of mineralized quartz veins and altered metavolcanic host rocks, respectively.

5. Remote sensing data analysis and results

In this study subsets of the ETM+ scene (Path 173/Row 45, acquired on March 09, 2005), and the medium resolution, cloud-free level 1B ASTER VNIR & SWIR data (Granule ID: ASTL1B 0403150819140808041013, acquired on March 15, 2008 from ERSDAC, Japan), have been processed using the ENVI v. 4.5 image processing and analysis software (ITT Visual Information Solutions). Image processing techniques including band ratioing, principal component analysis (PCA), false-color composition (FCC), and frequency-domain filtering (i.e., FFT-RWT) have been applied for detailed mapping of the lithological units, structures and alteration zones in the study area. The USGS spectral library (http://www.speclab.cr.usgs.gov) of rock forming minerals was used to evaluate the ETM+ and ASTER image spectral signatures, considering already identified mineral composition of the different lithological units in the study area.

5.1. Band ratioing

The band ratio transformation of TM and ASTER data is useful for qualitative detection of hydrothermal alteration minerals (Di Tommaso and Rubinstein, 2007), and also has wide acceptance in geological mapping in the Eastern Desert of Egypt (e.g., Qiu et al., 2006; Amer et al., 2010; Aboelkhair et al., 2010; Madani and Emam, 2011). Band ratios of ETM 5/7, 5/4 and 3/1 and their combinations in RGB sequence as images were created for the detection of hydrous minerals and iron-rich zones (e.g., Crosta and Moore, 1989; Bannari et al., 1995; Sabins, 1997, 1999). Clays in ASTER have absorption features mainly in shortwave infrared radiation subsystem (SWIR) bands 5 and 6, whereas carbonate absorption occurs in band 8, as do those in minerals with Mg–OH and Fe–OH ligands such as talc, chlorites and amphiboles (Abrams and Hook, 1995; Drury, 2001).

In this study, the produced images give either comparable or complementary results in most cases. The ETM+ band ratio (5/7) and ASTER band ratio (4/7) images (Fig. 4a and b) identify serpentinite and talc-rich rocks by a bright image signature, and further allow discrimination between the highly sheared, carbonatized, serpentinite and talc-carbonate schist from less-deformed (massive) serpentinite and ultramafites. Granitoid rocks have bright tones on the ETM+ band ratio (3/1) and ASTER band ratio (2/4) images, whereas, amphibolite and highly sheared ophiolites appear as dark gray or black pixels (Fig. 4c and d). Gabbro–diorite blocks in the southern part of the study area show dark gray image signature on the ETM+ band ratio (4/5) image compared to island arc metavolcanics, metasiltstone and carbonaceous schist and amphibolite are black zones, and serpentine- and talc-rich rocks define the major thrust structures by bright pixels (Fig. 4e). The island arc metavolcanics and gabbro–diorite have a pale gray image signature on the ASTER band ratio (6/8) image, granitoid intrusions

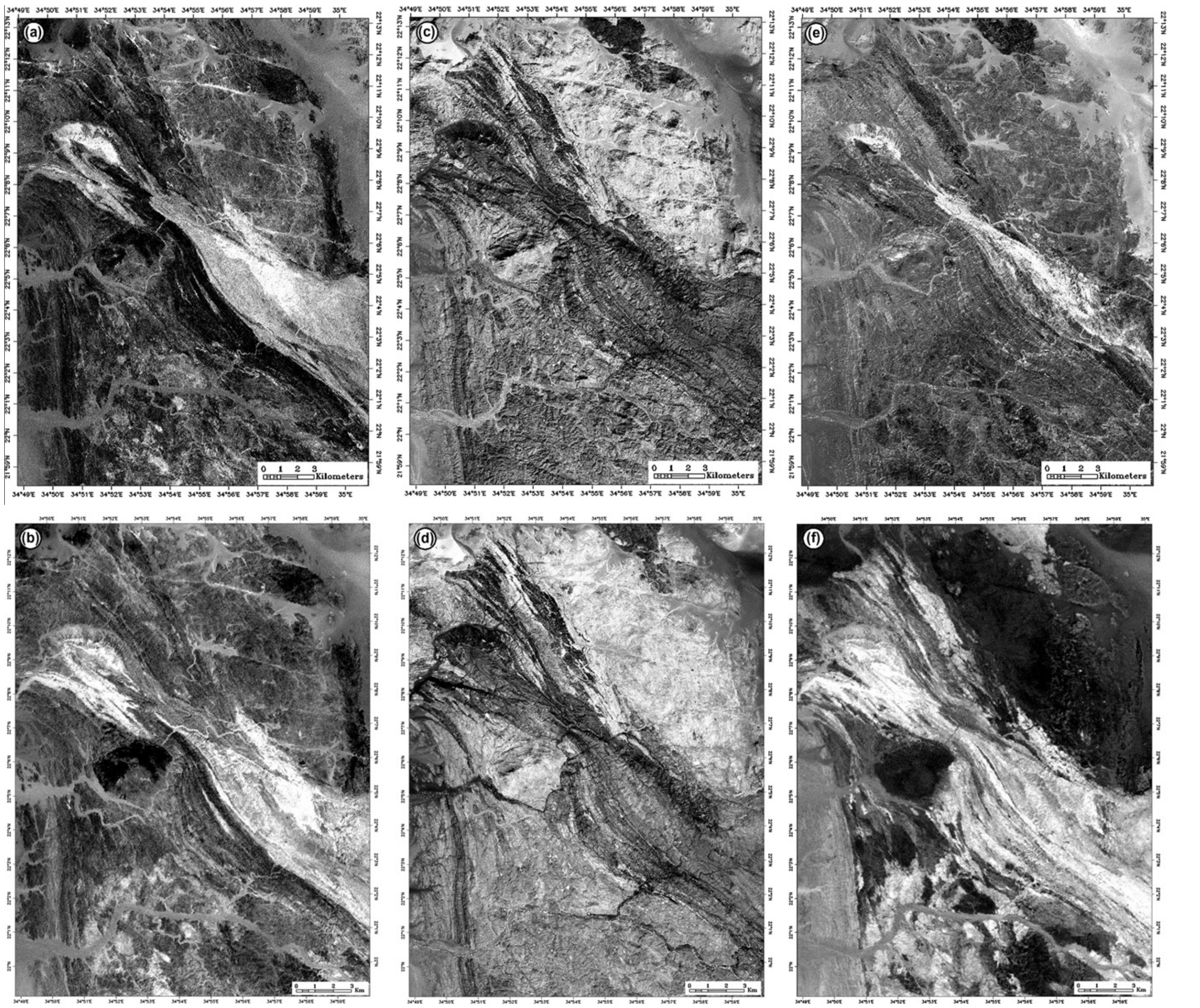

Fig. 4. (a) ETM+ band ratio (5/7) image, (b) ASTER Band ratio (4/7) image. Notice that carbonatized serpentinite and talc-carbonate schist appear as bright pixels, while massive serpentinite is solid white areas, (c) ETM+ band ratio (3/1) image discriminates the granitoid intrusions with bright tone, (d) ASTER band ratio (2/4) image shows similar features as in (c), but further enables identification of granitoid slabs along foliation the metagabbro belt close to the mining areas, (e) ETM+ band ratio (4/5) image, and (f) ASTER Band ratio (6/8) image discriminate between the mafic/ultramafic rocks (bright tone) from granitoids (dark tone).

show dark gray to black image signature and Fe-rich rocks (mafic–ultramafic rocks) are differentiated clearly with the bright tone(Fig. 4f).

5.2. Principal component analysis (PCA)

PCA is a multivariate statistical method which predicts whether the target material is represented as bright or dark pixels in the different principal components according to the magnitude and sign of the Eigenvector loadings (Jolliffe, 1986). According to Loughlin (1991), a PC image with moderate to high Eigenvector loadings for diagnostic reflective and absorptive bands of mineral or mineral group with opposite signs enhances that mineral. Eigenvector statistics in each PCA would, therefore, identify the PC image in which the spectral information of a mineral under examination is loaded. This information usually represents, in quantitative terms, a very small fraction of the total information content of the original bands, but it is expected that the loading information indicates the spectral signature of the desired mineral (Crosta and Moore, 1989; Loughlin, 1991).

PCA outputs are presented in Table 2 and selected PC images from these transformations are reproduced in Fig. 5 to support the discussion. PC1 is composed of positive weightings of all 6 ETM+ and 9 ASTER (VNIR + SWIR) bands. As indicated by the Eigenvalues, PC1 accounts for 95.34% and 98.59% of the total variance of ETM+ and ASTER data, respectively. Overall scene brightness, or albedo, is responsible for the strong correlation between multispectral image bands in PC1 (Loughlin, 1991). According to the Crosta and Moore (1989) approach, the magnitude and sign (positive or negative) of eigenvector loadings are indications of which spectral properties of surface materials (rocks, vegetation, and soils) are responsible for the statistical variance mapped into each PC.

ETM+ PC2 shows the difference between the visible and infrared bands, and contains 3.84% of the original data variance. PC2 has positive Eigenvector loading values for bands 1–4, while values for bands 5 and 7 are negative (Table 2). This is the contrast between visible and SWIR region in the image. It shows high positive eigenvector loadings for band 1 (0.442) and high negative eigenvector loadings for band 7 (−0.609). The OH-bearing minerals have opposite spectral characteristics in band 1 and in band 7. They have high reflectance in band 1 and high absorption in band 7, therefore, the alteration zones and rocks containing high contents of Al–OH and Mg–OH minerals are best discriminated with bright pixels on the ETM+ PC2 image of the study area (Fig. 5a). The ETM+ PC3 gives high positive eigenvector loadings for band 1 (0.588) and high negative eigenvector loadings for band 4 (−0.617) and band 3 (−0.301). It contains only 0.43% of the original data variance. The iron-stained or iron-rich rocks have high absorption in band 1 and high reflectance in bands 4 and 3. Carbonaceous schist metasiltstone and Fe-rich rocks (i.e., amphibolite, metagabbro and metabasalt) show bright image signatures, whereas silica-rich (granitoids) and Mg-rich (serpentinite and talc-carbonate) appear light gray (Fig. 5b). Sericitization, silicification zones in the mine sites are seen as dark slabs within the bright metagabbro belt (Fig. 5b). Hydroxyl minerals are enhanced in PC4 as this PC has higher loading of band 5, but with opposite sign for band 7. ETM+ PC4 has a positive contribution of band 5 (0.738) and a negative one of band 7 (-0.553). This is in accordance with spectral characteristics of OH-minerals that have reflectance in band 5 and absorption in band 7 (Clark, 1999). The ETM+ PC4 image identifies Mg–OH-rich rocks (i.e., serpentinite and talc-carbonate schist) in bright tones (Fig. 5c). The strongly foliated metagabbro belt appears in a darker tone, as well as the mylonite zone in the western part of the area. Hydrothermal alteration zones in the Egat and Al-Fawi mine sites are seen as narrow bright strips within the

Table 2
Eigenvector matrix and loadings of principal component analysis on ETM+ and ASTER data for G. Egat scene.

ETM+ bands	PC1	PC2	PC3	PC4	PC5	PC6
Band 1	0.406	0.442	0.588	0.277	0.454	0.110
Band 2	0.411	0.356	0.077	-0.115	-0.607	-0.563
Band 3	0.414	0.235	-0.301	-0.115	-0.286	0.755
Band 4	0.415	0.052	-0.617	-0.171	0.560	-0.317
Band 5	0.405	-0.499	-0.122	0.738	-0.167	-0.007
Band 7	0.398	-0.609	0.403	-0.553	0.048	0.021
Eigenvalues	2055.02	82.78	9.20	4.88	2.24	1.40
Information (%)	95.34	3.84	0.43	0.23	0.10	0.06

(VNIR and SWIR) bands		PC1	PC2	PC3	PC4	PC5	PC6	PC7	PC8	PC9
VNIR	Band 1	0.609	-0.675	0.234	0.344	-0.014	-0.027	0.001	0.000	0.001
	Band 2	0.632	-0.102	-0.328	-0.695	0.013	-0.002	-0.006	0.000	-0.001
	Band 3	0.468	-0.680	-0.069	0.558	0.016	0.046	0.003	0.002	0.000
SWIR	Band 4	0.095	-0.237	0.774	-0.254	-0.516	-0.054	0.023	-0.029	-0.012
	Band 5	0.025	-0.047	0.272	-0.086	0.411	0.405	-0.725	-0.203	0.123
	Band 6	0.025	-0.034	0.258	-0.094	0.415	0.569	0.641	0.116	0.050
	Band 7	0.025	-0.077	0.235	-0.065	0.426	-0.421	-0.127	0.722	-0.194
	Band 8	0.019	-0.066	0.161	-0.043	0.371	-0.539	0.192	-0.408	0.580
	Band 9	0.012	-0.035	0.110	-0.030	0.269	-0.195	0.101	-0.507	-0.780
Eigenvalues		1101.03	11.36	2.76	1.41	0.15	0.06	0.01	0.004	0.003
Information (%)		98.59	1.02	0.25	0.13	0.013	0.006	0.001	0.0004	0.0003

Cells shaded in yellow are the highest values and those in orange are moderate ones.

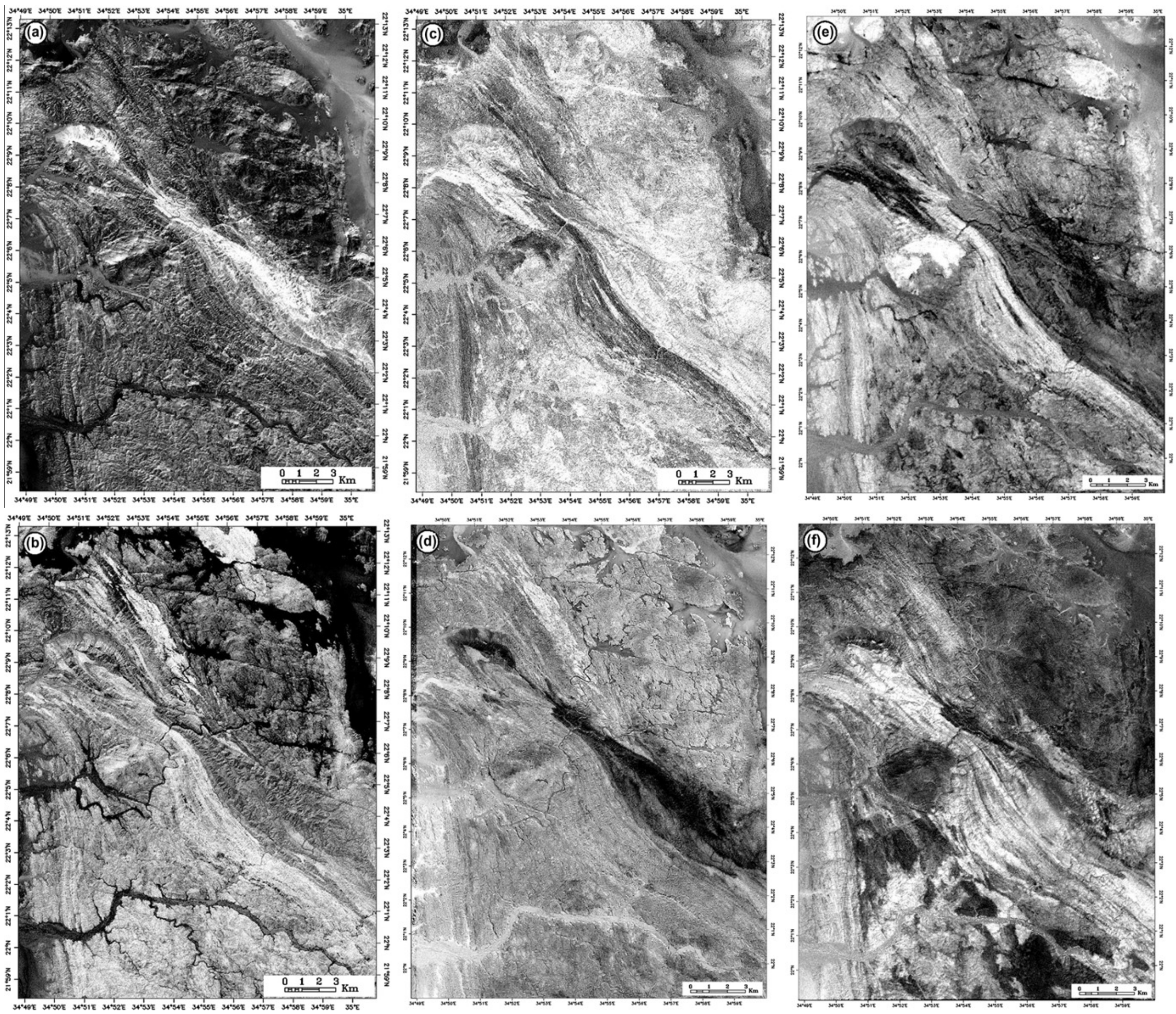

Fig. 5. Principal component resultant images on ETM+ and ASTER data of the G. Egat area. (a) ETM+ PC2, (b) ETM+ PC3, (c) ETM+ PC4, (d) ASTER PC3, (e) ASTER PC5, and (f) ASTER PC6. See the text for details and interpretations.

metagabbro belt, likely due to high contents of hydrous minerals (Fig. 5c).

Eigenvector loadings for all bands in ASTER PC2 are negative, suggesting that this PC is noisy and lacks any information (Table 2). By looking for high Eigenvector loadings for bands 2 and 4 in PCs where these loadings are also in opposite sign, we can predict that iron oxides can be distinguished by bright pixels in PC3. Iron oxide minerals have low reflectance in visible (band 2) and higher reflectance in near infrared (band 4) (e.g., Abdelsalam and Stern, 2000; Velosky et al., 2003). Iron-rich rocks can be mapped as bright pixels in PC3 because of the high positive contribution from band 4 (0.774) and negative contributions from band 2 (-0.328). Amphibolite and carbonaceous schist have bright signatures on the PC3 image (Fig. 5d). Distinctly, serpentinite and talc-carbonate schist (Mg–OH-rich rocks) appear in black and dark gray, respectively. Vegetation has high reflectance in band 3 and very low in band 2 of ASTER data (e.g., Ninomiya, 2003; Xu et al., 2004). PC4 is therefore, useless in this study.

According to spectral characteristics, ASTER band 4 covers the spectral region ($\sim$1.6 μm) where all OH-bearing minerals have maximum reflectance. Al(OH)-bearing minerals such as kaolinite, alunite, muscovite and illite show major absorption in bands 5, 6 and 7 (2.14–2.28 μm). Fe, Mg(OH)-bearing minerals such as chlorite, as well as carbonates such as calcite and dolomite are well covered in bands 8 and 9 (2.29–2.43 μm) of ASTER data (e.g., Crosta et al., 2003; Mars and Rowan, 2006). Considering the magnitude and sign of the Eigenvectors loadings and the percentage of variance, it is clear that PC5 and PC6 contain the target information. The remaining PCs (PC7–PC9) are noisy and uninformative in this study. PC5 contains only 0.013% of total variability of original data. It has high positive eigenvector loadings for band 7 (0.426) and high negative loadings for band 4 ($-$0.516). The PC5 image is clearly able to discriminate the OH-rich rocks (e.g., talc-carbonate, carbonatized ophiolites) and hydrothermal alteration zones by their dark gray to black signatures (Fig. 5e). PC6 contains only 0.006% of total variability of original data. It shows high positive eigenvector loadings for band 6 (0.569) and high negative loadings for band 8 ($-$0.539). It enables differentiation between the gabbroid–basaltic rocks by their bright image signature from granitoid rocks that appear as dark gray to black pixels (Fig. 5f).

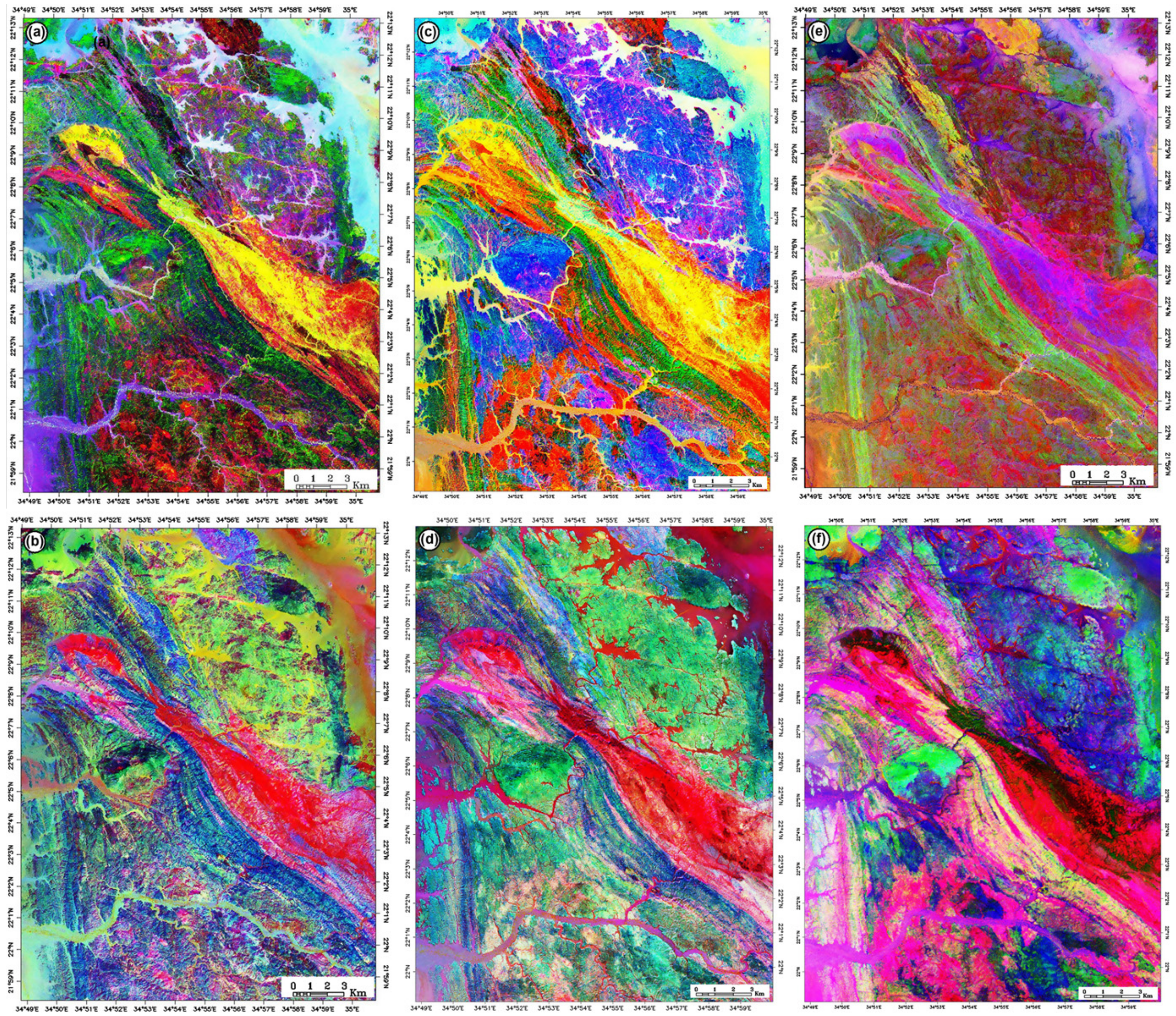

Fig. 6. RGB false color composite images (FCC) of ETM+ and ASTER data of the G. Egat area. (a) ETM+(5/7,4/5, 3/1) image, (b) ETM+(5/7, 5/1, 5/4 ∗ 3/4) image, (c) ASTER (4/7, 2/4, 6/8) image. (d) ASTER (4/7, 2/4, 6/8) image, (e) ETM+(PC4, PC3, PC2) FCC image, and (f) ASTER (PC6, PC5, PC3) FCC image of the Gebel Egat area. See the text for details and interpretations.

5.3. False-color composition (FCC)

The ETM+ 5/7–4/5–3/1 (Abrams et al., 1983) image shows carbonatized serpentinite and talc-carbonate schist in yellow, while orange delineates the mélange matrix and metabasalt appears in pale red (Fig. 6a). Amphibolite appears in dark red, and carbonaceous schist and marble yield mixed dark brown or black with light pink hue. According to Sultan et al. (1986), the 5/7 band ratio brings out argillite, serpentinite, and alteration zones in arid and semi-arid environments, and band 5/1 distinguishes mafic igneous rocks, while the ratio 5/4 ∗ 3/4 successfully discriminates mafic from felsic rocks. The ETM+ 5/7–5/1–5/4 ∗ 3/4 FCC image can efficiently discriminate granitoid from gabbroid rocks (Fig. 6b). Granodiorite and syenogranite are pale green and dark green, respectively, whereas metagabbro, gabbros and metabasalt appear as blue. Serpentinite and hydrothermal alteration zones are delineated with red and light red to rose image signature respectively, while the intermediate metavolcanics show purple color.

The ASTER 4/7–2/4–6/8 and 4/7–4/1–2/3 ∗ 4/3 FCC images are found most efficient in differentiating all lithologic units and hydrothermally altered zones in the study area (Fig. 6c and d), where serpentinite appears in yellow, talc-carbonates schist in light rose, metabasalt in red, metagabbro in brownish green, amphibolite and carbonaceous schist in reddish brown, metavolcanics in deep red, metavolcaniclastics in purple or whitish blue, gabbro–diorite in yellowish red, granitoids in blue, metapelites in dark blue, and mylonite in green. Silicification zones and quartz veins have light pinkish image signature (see Fig. 6c). On the ASTER 4/7–4/1–2/3 ∗ 4/3 image, granodiorite and syenogranite are better identified by their green[1] color from the quartz-diorite and metavolcaniclastic rocks, and alteration zones where foliation is wrapped around the Egat intrusion are more distinct as yellowish white zones (see Fig. 6d).

A false color composite (FCC) image created by combination of the ETM+ PCs (PC4, PC3 and PC2 as red, green and blue, respectively) shows the hydrothermal alteration zones in the mining sites

[1] For interpretation of color in Figs. 1–3, 6 and 7, the reader is referred to the web version of this article.

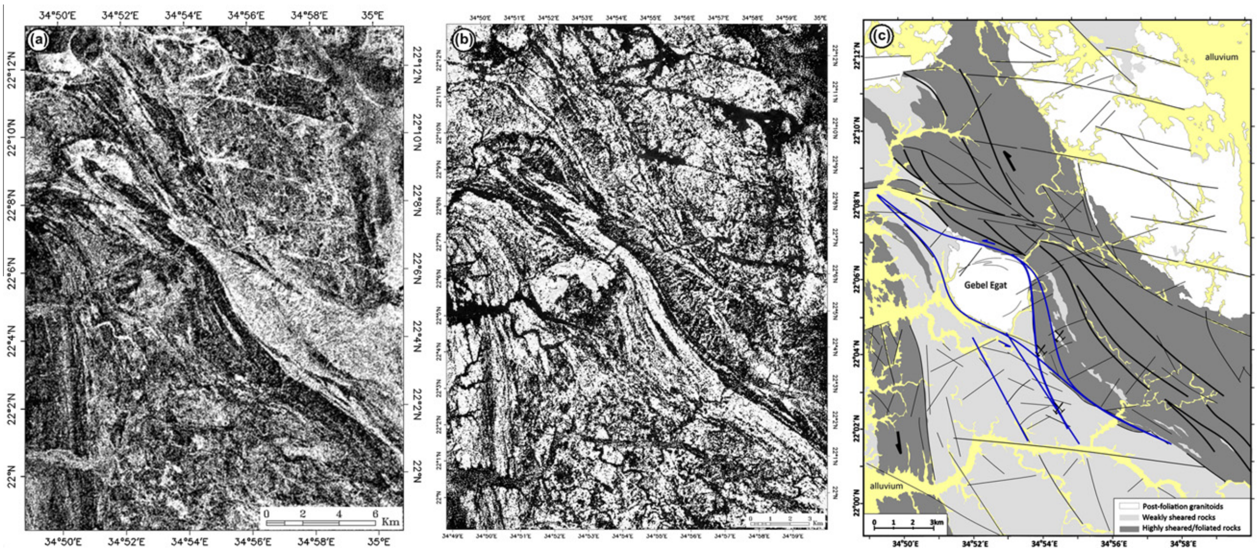

Fig. 7. (a) PC3-FFT-RWT ETM+ image, (b) PC5-FFT-RWT ASTER image of the G. Egat area, and (c) Interpretation map compiled from both produced images and field observations.

in red, and identifies potential hydrothermal alteration zones north of G. Egat (Fig. 6e). In addition, this image also discriminates between schistose/intensely sheared rocks from the weakly deformed rocks. A false color composite image using ASTER PCs (PC6, PC5, PC3 in red, green and blue, respectively; Fig. 6f) shows highly tectonized, listvenitized ophiolites in light red and rose, while the less deformed serpentinites appear in dark green. Granitoid rocks appear as purple and light blue colors. The lemon color on the northern part of the Egat syenogranite body is attributed to roof-pendants and abundant xenoliths of metagabbro. The metagabbros and metabasalts give light yellowish and pinkish tones, respectively. The arc metavolcanics (mostly basic) appear as rose, gabbro–diorite as pale green, and quartz-diorite as dark blue. In the south-western part, metapelites appear in white and mylonite in yellowish white (Fig. 6f).

5.4. Frequency filtering techniques

The Discrete Fourier Transform (DFT) is a specific form of Fourier analysis to convert one function (often in the time or spatial domain) into another (frequency domain). It is widely employed in signal processing and related fields to analyze frequencies contained in a sample signal, to solve partial differential equations, and to perform other operations such as convolutions (Duhamel and Vetterli, 1990). In the field of satellite image processing, DFT is a useful approach for suppressing artificial signals produced by the random high frequency noise generated from PCA, and to remove periodic features, such as striping (Gonzalez and Woods, 2002).

Fast Fourier Transform (FFT) is an efficient implementation of DFT and is generally used in digital image processing. Applying filters to images in the frequency domain is computationally faster than to do the same in the image domain (Srinivasan et al., 1988). The FFT provides better visual interpretation of the image for the purpose of extracting structural information, while the richness in spectral information in the RGB color combination image can sometimes mask structural continuity a challenging task in areas showing structural complexity (e.g., Ren and Abdelsalam, 2006). The ETM+ PC3 (Fig. 5b) and ASTER PC5 (Fig. 5e) images appear to emphasize regional structural trends relative to spectral variations. Therefore, they have been selected for applying the frequency filtering to trace the geological structures (e.g., Richards and Jia, 1999; Ren and Abdelsalam, 2006). Three steps are carried out to apply the frequency filtering for these PC images. In the first step, the ETM+ PC3 and ASTER PC5 are converted into frequency domain images using the FFT technique. The second step comprises designing a low-pass circular filter, which will retain or eliminate data with desired frequencies in order to reduce the high frequency noise in the frequency domain images. In the third step, the inverse FFT is applied to transfer the frequency-filtered information back into spatial domain images.

Redundant Wavelet Transform (RWT) is a wavelet transform, in which pixel dimensions remain the same and includes no down- or up-resampling (Brown, 2000). The RWT is used to enhance and sharpen the resultant FFT images. In order to enhance the image contrast, amplification of the wavelet coefficients by using the algorithm of Zong et al. (1996) was applied. This algorithm typically includes the use of non-linear mapping functions to process the wavelet coefficients (Zong et al., 1996; Brown, 2000). The resultant enhanced images (Fig. 7a and b) are found to best show linear features and regional structures in the study area. The interpretation map (Fig. 7c) shows a major sigmoidal pattern around the G. Egat intrusion, suggesting sinistral transpression and up-to-left rotation concomitant with granite emplacement.

6. Discussion and conclusions

Based on the characteristic criteria described by Groves et al. (1998), gold lodes in the Egat–Al-Fawi area are believed to be orogenic (Zoheir et al., 2008). A prominent characteristic of orogenic gold lodes is their occurrence in greenstone belt proximal to trans-lithospheric structures, i.e. at major tectonic boundaries of metamorphosed volcanic–plutonic or sedimentary terrains. Our field observations and space-borne data interpretations indicate that the anastomosing set of NNW–SSE shear zones in the Egat mine area are splays off the major N–S, Hamisana Zone (Stern et al., 1989; Miller and Dixon, 1992; Greiling et al., 1994; de Wall et al., 2001). Elsamani et al. (2001) located more than 15 occurrences of shear-related auriferous quartz veins within the Hamisana Zone in north Sudan. According to the metamorphic model for gold deposits (Groves and Phillips, 1987), gold was leached out from the greenstone rocks by infiltrating hydrothermal (metamorphic) fluids and deposited in pervasive structures due to physicochemical gradients (Eh, pH, pressure–temperature variations) between the first-and second-order structures (e.g., Eisenlohr et al., 1989; Ridley, 1993; Kolb et al., 2000). Heat from granite intrusions may produce convection cells and drive active hydrothermal (mostly metamorphic) fluids to circulate into and leach metals from the foliated greenstone belts (e.g., Craw and Norris, 1991; McCuaig and Kerrich, 1998; Thébaud et al., 2008).

Gold lodes and hydrothermal alteration zones at Egat and Al-Fawi mining sites are confined to dilatation zones produced by foliation deflection throughout a sinsitral transpressional regime. Development of the mineralized shear zones is likely to have been contemporaneously with granitic diapirism and greenschist-grade metamorphism. Orebodies in the study area are stretched parallel to the stretching lineation, suggesting a syn-tectonic genesis of quartz veining/gold mineralization. Irregularities along shear zones and pull-apart structures are developed parallel to the lineation by displacement of competent patches of the host rocks. Domains of intensely sheared rocks are mainly the structural contact between island arc metavolcanics and ophiolites or quartz diorite, especially where dyke-like granitoid bodies are tapered along S_2 foliation.

Integrated image transformation methods (e.g., band ratioing, PCA, FCC and FFT-RWT) on selective bands of the ETM and ASTER data, have been found to be self-calibrating, scene-dependent, and complimenting each other for identification of lithologies and hydrothermal altered zones. In addition, highlighting the intensely deformed/sheared rocks in the area aided understand the setting of gold-quartz lodes in relation to the Egat intrusion.

Because of the relatively large size of porphyry copper and epithermal gold mineralization economic geologists can benefit from different image processing techniques in exploring for new prospects. In the case of orogenic gold lodes in vast terrains, setting a model or characterizing a setting is a challenging job for which the remote sensing techniques that we have discussed would certainly assist exploration programs. Resulting from our study, highly foliated belts of stacked ophiolites that are cut by granitic stocks showing signs of emplacement throughout transpression are suggested as a model for hydrothermal gold exploration targets (i.e., orogenic gold lodes) in the greenstone terrain of the South Eastern Desert. Similar gold mineralization associated with granitoid intrusions in transpression-induced pull-apart structures in the Fawakhir, Hangaliya and Sukari gold mines (e.g., Loizenbauer and Neumayr, 1996; Surour et al., 2001; Helmy et al., 2004) add credence to the Egat gold lodes' setting as a model for gold exploration targets in the Eastern Desert of Egypt, and maybe elsewhere in the Arabian–Nubian Shield.

Acknowledgments

This study was financially supported by the Science and technology development fund (STDF), Egypt. Dr. A. Drury and an anonymous reviewer are thanked for help in improving the early version of this manuscript.

References

Abdeen, M.M., Abdelghaffar, A.A., 2011. Syn- and post-accretionary structures in the Neoproterozoic Central Allaqi-Heiani suture zone. Southeastern Egypt. Precambrian Research 185 (3–4), 95–108.
Abdelsalam, M., Stern, R., 2000. Mapping gossans in arid regions with landsat TM and SIR-C images, the Beddaho Alteration Zone in northern Eritrea. Journal of African Earth Sciences 30 (4), 903–916.
Aboelkhair, H., Yoshiki, N., Yasushi, W., Isao, S., 2010. Processing and interpretation of ASTER TIR data for mapping of rare-metal-enriched albite granitoids in the Central Eastern Desert of Egypt. Journal of African Earth Sciences 58 (1), 141–151.
Abrams, M.J., Brown, D., Lepley, L., Sadowski, R., 1983. Remote sensing for porphyry copper deposits in Southern Arizona. Economic Geology 78, 591–604.
Abrams, M., Hook, S.J., 1995. Simulated ASTER data for geologic studies. IEEE Transactions on Geoscience and Remote Sensing 33 (3).
Amer, R., Kusky, T., Ghulam, A., 2010. Lithological mapping in the Central Eastern Desert of Egypt using ASTER data. Journal of African Earth Sciences 56, 75–82.
Ashley, P.M., Craw, D., 2004. Structural controls on hydrothermal alteration and gold antimony mineralization in the Hillgrove area, NSW, Australia. Mineralium Deposita 39, 223–239.
Bannari, A., Morin, D., Bonn, F., 1995. A review of vegetation indices. Remote Sensing Reviews 13, 95–120.
Bierlein, F.P., Crowe, D.E., 2000. Phanerozoic orogenic lode gold deposits. In: Hagemann, S.G., Brown, P.E. (Eds.), Gold in 2000. Society of Economic Geologists Reviews in Economic Geology, vol. 13. pp. 103–139.
Brown, T.J., 2000. An adaptive strategy for wavelet based image enhancement. In: Proceedings of Irish Machine Vision and Image Processing (IMVIP) Conference, pp. 67–81.
Clark, R.N., 1999. Manual of remote sensing. In: Rencz, A.N. (Ed.), Remote Sensing for the Earth Sciences, vol. 3. John Wiley and Sons, New York, pp. 3–58.
Craw, D., Norris, R.J., 1991. Metamorphogenic Au–W veins and regional tectonics: mineralisation throughout the uplift history of the Haast Schist, New Zealand. New Zealand Journal of Geology and Geophysics 34, 373–383.
Craw, D., Windle, S.J., Angus, P.V., 1999. Gold mineralization without quartz veins in a ductile–brittle shear zone, Macraes Mine, Otago Schist, New Zealand. Mineralium Deposita 34, 382–394.
Crosta, A.P., Moore, J.M., 1989. Enhancement of Landsat Thematic Mapper imagery for residual soil mapping in SW Minais Gerais State, Brazil: a prospecting case history in Greenstone belt terrain. In: Proceedings of the 7th ERIM Thematic Conference. Remote Sensing and Exploration Geology, pp. 1173–1187.
Crosta, A.P., Souza Filho, C.R., Azevedo, F., Brodie, C., 2003. Targeting key alteration minerals in epithermal deposits in Patagonia, Argentina, Using ASTER imagery and principal component analysis. International Journal of Remote Sensing 24, 4233–4240.
de Wall, H., Greiling, R.O., Sadek, M.F., 2001. Post-collisional shortening in the late Pan-African Hamisana high strain zone, SE Egypt: field and magnetic fabric evidence. Precambrian Research 107, 179–194.
de Wit, M.J., Ashwal, L.D., 1995. Greenstone Belts: what are they? South African Journal of Geology 98, 505–520.
Di Tommaso, I., Rubinstein, N., 2007. Hydrothermal alteration mapping using ASTER data in the Infiernillo porphyry deposit, Argentina. Ore Geology Reviews 32, 275–290.
Drury, S.A., 2001. Image Interpretation in Geology. Nelson Thornes Blackwell Science, Cheltenham Malden, 290pp.
Duhamel, P., Vetterli, M., 1990. Fast Fourier transforms: a tutorial review and a state of the art. Signal Processing 19, 259–299.
Eisenlohr, B.N., Groves, D., Partington, G.A., 1989. Crustal-scale shear zones and their significance to Archaean gold mineralization in Western Australia. Mineralium Deposita 24, 1–8.
Elsamani, Y., Al-Muslem, A., El Tokhi, M., 2001. Geology and geotectonic classification of Pan-African gold mineralizations in the Red Sea Hills, Sudan. International Geology Review 43, 1117–1128.
Gabr, S., Ghulam, A., Kusky, T., 2010. Detecting areas of high-potential gold mineralization using ASTER data. Ore Geology Reviews 38(1–2), 59–69.
Goldfarb, R.J., Groves, D.I., Gardoll, S., 2001. Orogenic gold and geologic time: a global synthesis. Ore Geology Reviews 18, 1–75.
Gonzalez, R.C., Woods, R.E., 2002. Digital Image Processing, second ed. Prentice-Hall, Englewood Cliffs, NJ, 793pp.
Greiling, R.O., Abdeen, M.M., Dardir, A.A., El Akhal, H., El Ramly, M.F., Kamal El Din, G.M., Osman, A.F., Rashwan, A.A., Rice, A.H.N., Sadek, M.F., 1994. A structural synthesis of the Proterozoic Arabian–Nubian shield in Egypt. Geologische Rundschau 83, 484–501.
Groves, D.I., Goldfarb, R.J., Gebre-Mariam, M., Hagemann, S., Robert, F., 1998. Orogenic gold deposits: a proposed classification in the context of their crustal distribution and relationship to other gold deposit types. Ore Geology Reviews 13, 7–27.
Groves, D.I., Phillips, G.N., 1987. The genesis and tectonic controls on Archaean Gold deposits of the Western Australian Shield: a metamorphic-replacement model. Ore Geology Reviews 2, 287–322.
Helmy, H.M., Kaindl, R., Fritz, H., Loizenbauer, J., 2004. The Sukari Gold Mine, Eastern Desert, Egypt: structural setting, mineralogy and fluid inclusion study. Mineralium Deposita 39, 495–511.
Hodgson, C.J., 1993. Mesothermal lode-gold deposits. In: Kirkham, R.V., Sinclair, W.D., Thorpe, R.I., Duke, J.M. (Eds.), Mineral Deposit Modeling. Geological Association of Canada, Special Paper, vol. 40, pp. 635–678.
Jolliffe, I.T., 1986. Principal Component Analysis. Springer-Verlag. 487pp.
Kolb, J., Kisters, A.F.M., Hoernes, S., Meyer, F.M., 2000. The origin of fluids and nature of fluid–rock interaction in midcrustal auriferous mylonites of the Renco mine, southern Zimbabwe. Mineralium Deposita 35, 109–125.
Kusky, T.M., Ramadan, T.M., 2002. Structural controls on Neoproterozoic mineralization in the South Eastern Desert, Egypt: an integrated field, Landsat TM and SIR-C/X SAR approach. Journal of African Earth Sciences 35, 107–121.
Loizenbauer, J., Neumayr, P., 1996. Structural controls on the formation of the Fawakhir gold mine, El Sid-Eastern Desert, Egypt: tectonic and fluid inclusion evidence. In: Proceedings of the Geological Survey of Egypt Centennial Conference, pp. 477–488.
Loughlin, W.P., 1991. Principal components analysis for alteration mapping. Photogrammetric Engineering and Remote Sensing 57, 1163–1169.

Madani, A., Emam, A., 2011. SWIR ASTER band ratios for lithological mapping and mineral exploration: a case study from El Hudi area, Southeastern Desert, Egypt. Arabian Journal of Geosciences 4, 45–52.

Mars, J.C., Rowan, L.C., 2006. Regional mapping of phyllic- and argillic altered rocks in the Zagros magmatic arc, Iran, using Advanced Spaceborne Thermal Emission and Reflection Radiometer (ASTER) data and logical operator algorithms. Geosphere 2 (3), 161–186.

McCuaig, T.C., Kerrich, R., 1998. P–T–t deformation fluid characteristics of lode-gold deposits: evidence from alteration systematics. Ore Geology Reviews 12, 381–453.

Miller, M.M., Dixon, T.H., 1992. Late Proterozoic evolution of the northern part of the Hamisana zone, northeast Sudan: constraints on Pan-African accretionary tectonics. Journal of the Geological Society, London 149, 743–750.

Nasr, B.B., Masoud, M.S.El., Sherbeni, H., Makhlof, A.A., 1998. Some new occurrences of gold mineralization, Eastern Desert, Egypt. Annals of the Geological Survey of Egypt 21, 331–344.

Ninomiya, Y., 2003. A stabilized vegetation index and several mineralogic indices defined for ASTER VNIR and SWIR data. In: Proceeding of the IEEE 2003 International Geosciences and Remote Sensing Symposium (IGARSS'03), vol. 3. Toulouse, France, 21–25 July, pp. 1552–1554.

Osman, A., Dardir, A., 1989. On the mineralogy and geochemistry of some gold-bearing quartz veins in the central Eastern Desert of Egypt and their alteration wallrocks. Annals Geological Survey Egypt 16, 17–25.

Oweiss, K.A., Khalid, A.M., 1991. Geochemical prospecting at Um Qareiyat gold deposits, South Eastern Desert, Egypt. Annals Geological Survey of Egypt 17, 145–151.

Oweiss, Kh.A., Said, M.M., 2000. Geological and geochemical exploration for gold at Um Egat (Al Fawi) area, south Eastern Desert, Egypt. Annals of the Geological Survey of Egypt 23(2), 609–613.

Qiu, F., Abdelsalam, M.G., Thakkar, P., 2006. Spectral analysis of ASTER data covering part of the Neoproterozoic Allaqi-Heiani suture, southern Egypt. Journal of African Earth Sciences 44, 169–180.

Ramadan, T.M., Abdelsalam, M.G., Stern, R.J., 2001. Mapping gold-bearing massive sulfide deposits in the Neoproterozoic Allaqi Suture, Southeast Egypt with Landsat TM and SIR-C/X SAR images. Photogrammetric Engineering & Remote Sensing 67 (4), 491–497.

Ramadan, T.M., Kontny, A., 2004. Mineralogical and structural characterization of alteration zones detected by orbital remote sensing at Shalatein District area, SE Desert. Egypt. Journal of African Earth Sciences 40, 89–99.

Ren, D., Abdelsalam, M.G., 2006. Tracing along-strike structural continuity in the Neoproterozoic Allaqi-Heiani suture, southeastern Egypt using principal component analysis (PCA), fast Fourier transformation (FFT), and redundant wavelet transformation (RWT) of ASTER data. Journal of African Earth Sciences 44, 181–195.

Richards, J.A., Jia, X., 1999. Remote Sensing Digital Image Analysis—An Introduction, third ed. Springer-Verlag, Berlin, 363pp.

Ridley, J.R., 1993. The relations between mean rock stress and fluid flow in the crust: with reference to vein- and lode-style gold deposits. Ore Geology Reviews 8, 23–37.

Sabins, F.F., 1997. Remote sensing strategies for mineral exploration. In: Rencz, A.E. (Ed.), Remote Sensing for the Earth Sciences. John Wiley & Sons, Inc., New York, pp. 375–447.

Sabins, F.F., 1999. Remote sensing for mineral exploration. Ore Geology Reviews 14, 157–183.

Salem, S.M., 2007. Using remote sensing techniques in the geology and gold mineralization at Al Faw Eqat area, South Eastern Desert, Egypt. Egyptian Journal of Remote Sensing and Space Sciences 10, 137–150.

Srinivasan, R., Cannon, M., White, J., 1988. Landsat data destriping using power spectral filtering. Optical Engineering 27 (11), 939–943.

Stern, R.J., 1994. Arc assembly and continental collision in the Neoproterozoic East African Orogen: implications for the consideration of Gondwanaland. Annual Reviews Earth and Planetary Science Letters 22, 319–351.

Stern, R.J., Kröner, A., Manoton, W.I., Reischmann, T., Mansour, M., Hussein, I.M., 1989. Geochronology of the late Precambrian Hamisana shear zone, Red Sea Hills, Sudan and Egypt. Journal of the Geological Society, London 146, 1017–1029.

Sultan, M., Arvidson, R.E., Sturchio, N.C., 1986. Mapping of serpentinites in the Eastern Desert of Egypt using Landsat Thematic Mapper data. Geology 14, 995–999.

Surour, A.A., El-Bayoumi, R.M., Attawiya, M.Y., El-Feky, M.G., 2001. Geochemistry of wall rock alterations and radioactive mineralization in the vicinity of Hangaliya uraniferous shear zone, Eastern Desert, Egypt. Egyptian Journal of Geology 45 (1), 187–212.

Thébaud, N., Philippot, P., Rey, P., Brugger, J., Van Kranendonk, M., Grassineau, N., 2008. Protracted fluid–rock interaction in the Mesoarchaean and implication for gold mineralization: example from the Warrawoona syncline (Pilbara, Western Australia). Earth and Planetary Science Letters 272, 639–655.

Velosky, J.C., Stern, R.J., Johnson, P.R., 2003. Geological control of massive sulfide mineralization in the Neoproterozoic Wadi Bidah shear zone, southwestern Saudi Arabia, inferences from orbital remote sensing and field studies. Precambrian Research 123 (2–4), 235–247.

Xu, Y., Qizhong, L., Yun, S., Lu, W., 2004. Extraction mechanism of alteration zones using ASTER imagery. IEEE 2004, 4174–4175.

Zoheir, B.A., 2004. Gold Mineralization in the Um El Tuyor Area, South Eastern Desert, Egypt: Geologic Context, Characteristics and Genesis: Unpublished Ph.D. Thesis, Germany, Ludwig-Maximilians-Universität München, 159pp.

Zoheir, B.A., 2008. Structural controls, temperature–pressure conditions and fluid evolution of orogenic gold mineralisation in Egypt: a case study from the Betam gold mine, south Eastern Desert. Mineralium Deposita 43, 79–95.

Zoheir, B.A., 2011. Transpressional zones in ophiolitic mélange terranes: potential exploration targets for gold in the South Eastern Desert, Egypt. Journal of Geochemical Exploration 111, 23–38.

Zoheir, B.A., El-Shazly, A.K., Helba, H., Khalil, K.I., Bodnar, R.J., 2008. Origin and evolution of the Um Egat and Dungash orogenic gold deposits, Egyptian eastern desert: evidence from fluid inclusions in quartz. Economic Geology 103, 405–424.

Zoheir, B.A., Klemm, D.D., 2007. The tectonometamorphic evolution of the central part of the Neoproterozoic Allaqi-Heiani suture, south Eastern Desert of Egypt. Gondwana Research 12, 287–304.

Zong, X., Laine, A.F., Geiser, E.A., Wilson, D.C., 1996. De-noising and contrast enhancement via wavelet shrinkage and non-linear adaptive gain. Wavelet Applications 3. Proceedings of SPIE 2726, 566–574.